INTERNATIONAL JOURNAL FOR NUMERICAL METHODS IN FLUIDS
Int. J. Numer. Meth. Fluids 2009; **60**:611–631
DOI: 10.1002/fld.1904

A fully 3D finite element model for non-hydrostatic coastal flows with a free surface

Jordi Blasco[1,*,†], M. Augusto Maidana[2] and Manuel Espino[2]

[1]*Departament de Matemàtica Aplicada I, Univ. Politècnica de Catalunya, Campus Sud, Edfici H,*
Avgda. Diagonal 647, 08028 Barcelona, Spain
[2]*Laboratorio de Ingeniería Marítima, Univ. Politècnica de Catalunya, Campus Nord, Edfici D1,*
c/Gran Capità s/n, 08034 Barcelona, Spain

SUMMARY

In this paper we develop a finite element model, named HELIKE, for the numerical simulation of 3D, non-hydrostatic, turbulent flows with a free surface like those arising from the study of the motion of water in coastal regions. The kinematic free-surface equation is used to compute the surface elevation, without resorting to vertical averages. The model presented here incorporates surface wind stress, bottom friction and Coriolis acceleration, and it is applicable to irregular bottom topographies. A pressure stabilization technique is employed to stabilize the finite element solution. Numerical results obtained both in test problems and in a real-life application confirm the accuracy, robustness and applicability of the proposed method. Copyright © 2008 John Wiley & Sons, Ltd.

Received 5 October 2007; Revised 1 May 2008; Accepted 13 July 2008

KEY WORDS: kinematic free-surface equation; non-hydrostatic flows; finite elements; coastal flows

1. INTRODUCTION

The numerical modelling of the motion of water in coastal regions is a difficult and challenging problem due to the complexity of the different phenomena that affect the flow, the different time and space scales at which they occur and the irregularity of the geometries in which it takes place (see [1]). Moreover, it is a problem of great practical interest in different disciplines such as harbor engineering, the protection of beaches, water quality assessments and environmental flow problems.

---

[*] Correspondence to: Jordi Blasco, Departament de Matemàtica Aplicada I, Univ. Politècnica de Catalunya, Campus Sud, Edfici H, Avgda. Diagonal 647, 08028 Barcelona, Spain.

[†] E-mail: jorge.blasco@upc.edu

Contract/grant sponsor: Spanish MEC; contract/grant numbers: MTM2005-07660-C02-01, MTM2006-07932
Contract/grant sponsor: MODEGG; contract grant/number: CTM2005-05410-C03-01

Early numerical models for ocean dynamics were based on simplifying assumptions that limited their range of validity. Thus, a mixed finite element formulation was applied to solve the quasi-geostrophic equations in a two-layered ocean enclosed by solid boundaries in [2]. However, the increase in computer power over the last years has enabled more general, accurate and sophisticated models to be developed. In addition, the hydrostatic pressure assumption was extensively used in the past to obtain simplified models from the complete Navier–Stokes equations. The hydrostatic shallow water equations are still commonly used to study the circulation in well-mixed shallow estuaries, coastal seas and lakes (see [3–10]). On the other hand, the hydrostatic primitive equations of the ocean have also been extensively used especially in modelling large scale ocean dynamics (see [11–14]). However, the hydrostatic pressure approximation is not always valid for flows over rapidly varying slopes, such as littoral areas, and for short waves where the ratio of the vertical to the horizontal scales of motion is not sufficiently small; there are many important small-scale phenomena in the ocean (taking place at scales smaller than 1 km) such as wind- and buoyancy-driven turbulence in the surface mixed layers, large density gradients or convection in the open sea, which are not in hydrostatic balance and are fundamentally non-hydrostatic. We will focus on non-hydrostatic models in what follows.

The need to accurately predict the evolution of small surface gravity waves and to model tidal flows makes it necessary to incorporate an equation for the evolution of the free-surface elevation. Several other effects such as Coriolis acceleration, wind stress and bottom friction should also be accounted for, and a 3D formulation is mandatory for a versatile model. Several models incorporating all these phenomena have been developed so far.

As far as the numerical method employed to discretize the problem, most of the existing 3D non-hydrostatic, free-surface models use the finite difference method with a careful choice of the position of the velocity and pressure degrees of freedom on different cell locations [15–20]; other models use the finite volume method [21]. Nowadays, however, the finite element approach has become a useful tool in almost all areas of computational mechanics, and certainly in computational fluid dynamics, due to some properties of the method such as conservation of mass and energy, natural treatment of boundary conditions and flexibility of triangulation. To our knowledge, only a few 3D non-hydrostatic, free-surface finite element models have been developed so far, such as those of Causin *et al.* [22], Labeur and Pietrzak [23] and Walters [24, 25]. The FINEL3D model of Labeur and Pietrzak [23] does not incorporate Coriolis accelerations, surface wind stress, bottom friction nor an equation for the free surface. Both this model and the model of Causin *et al.* [22] use only constant values for the turbulent viscosity coefficients. Moreover, these models, as well as the models of Walters [24], are based on mixed finite element spatial discretizations with different interpolations for the velocity and the pressure, so as to satisfy the discrete inf–sup compatibility condition for the approximating spaces of the two variables: the MINI element in [23] and the lowest order non-conforming Raviart–Thomas element in [22, 24]. However, stabilized formulations like those of [26–30] have been shown to be more efficient than mixed interpolations for the numerical solution of incompressible flow problems (see [31]).

In this paper we develop a 3D, non-hydrostatic finite element model, named HELIKE, for coastal oceanic flows. This model incorporates Coriolis accelerations, surface wind stress, bottom friction and different turbulence closure models, and it is applicable to irregular bottom topographies. A stabilization technique based on a pressure gradient projection (PGP) (see [32–35]) is employed to avoid pressure oscillations, allowing the use of equal interpolation for the velocity and the pressure. We consider both a rigid-lid version of the model and a more complete version, which incorporates an evolution equation for the free-surface height. The original kinematic free-surface equation, rather than a vertically averaged form of it, is considered in our model, which exploits the possibility of using unstructured meshes both in the horizontal and in the vertical inherent to the finite element method. Prismatic elements with a triangular base are used for the spatial approximation, and an implicit (and therefore unconditionally stable) backward Euler method is employed for the time advancement.

The outline of the paper is as follows: Section 2 introduces the mathematical problem to be solved, which models the hydrodynamics of coastal regions. In Section 3 details are provided concerning the numerical scheme used to approximate the mathematical model; the time approximation is introduced first, followed by a description of the finite element method used for the spatial discretization and the technique employed to stabilize the pressure solution, since only equal-order approximations for the velocity and the pressure are considered and they can yield unphysical solutions when combined with standard Galerkin methods. In Section 4 some numerical results obtained with the proposed model on test cases and on a real-life application are given. Finally, some conclusions are drawn.

2. HYDRODYNAMICAL MODEL

In order to study the dynamics of water in coastal regions, we consider a 3D domain Ω defined by the equation:

$$\Omega = \{(x, y, z) \in \mathbb{R}^3 / (x, y) \in S, -\mathscr{H}(x, y) < z < 0\}$$

referred to Cartesian coordinates x, y (horizontal, with positive x eastbound and positive y northbound) and z (vertical), where $S \subset \mathbb{R}^2$ is the reference fluid surface (lying in the plane $z=0$) and $\mathscr{H}: \bar{S} \to \mathbb{R}$ is a positive function representing the bathymetry of the region of interest. The boundary of Ω can be decomposed as $\partial\Omega = \Gamma_s \cup \Gamma_b \cup \Gamma_l$, where

$$\Gamma_s = S \times 0 \quad \text{(the surface)}$$

$$\Gamma_b = \{(x, y, z) \in \mathbb{R}^3 / (x, y) \in S, -\mathscr{H}(x, y) = z\} \quad \text{(the bottom)}$$

$$\Gamma_l = \{(x, y, z) \in \mathbb{R}^3 / (x, y) \in \partial S, -\mathscr{H}(x, y) \leqslant z \leqslant 0\} \quad \text{(the lateral boundary)}$$

The motion of an incompressible, isopicnical fluid occupying Ω is governed by the 3D unsteady, incompressible Navier–Stokes equations expressed in a rotating coordinate system:

$$\frac{\partial \mathbf{u}}{\partial t} + (\mathbf{u} \cdot \nabla)\mathbf{u} + \mathbf{k} \times \mathbf{u} + \nabla P - \frac{\partial}{\partial x}\left(\nu_{\mathrm{H}} \frac{\partial \mathbf{u}}{\partial x}\right) - \frac{\partial}{\partial y}\left(\nu_{\mathrm{H}} \frac{\partial \mathbf{u}}{\partial y}\right) - \frac{\partial}{\partial z}\left(\nu_{\mathrm{V}} \frac{\partial \mathbf{u}}{\partial z}\right) = -\mathbf{g} \quad \text{in } \Omega \times (0, T) \tag{1}$$

$$\nabla \cdot \mathbf{u} = 0 \quad \text{in } \Omega \times (0, T) \tag{2}$$

where $\mathbf{u} = (u, v, w)$ is the 3D velocity of the fluid (as usual, boldface characters denote vector fields) and $P(x, y, z, t)$ is the fluid kinematic pressure, that is, the pressure divided by the fluid density ρ. The unknowns $\mathbf{u}$ and P are functions of the spatial coordinates $(x, y, z) \in \Omega$ and time $t \in (0, T)$, with $T > 0$ a given final time. Moreover, $\nabla = (\partial/\partial x, \partial/\partial y, \partial/\partial z)$ is the 3D gradient operator; $\mathbf{k} = (0, b, f)$, where $f = 2\omega \sin(\phi)$ and $b = 2\omega \cos(\phi)$ are the normal and the tangential Coriolis parameters, respectively, ω is the Earth's angular velocity and ϕ the latitude of the region

DOI: 10.1002/fld

of interest; ν_{H} and ν_{V} are the horizontal and vertical turbulent eddy viscosities, respectively; finally, $\mathbf{g}=(0,0,g)$, and g is the gravitational acceleration.

In non-hydrostatic models, Mahadevan *et al.* [36] advise to retain the vertical Coriolis acceleration that arises from the tangential component of the Coriolis parameter $b=2\omega\cos(\phi)$, commonly neglected in hydrostatic models. This component of the Coriolis acceleration is a dominant term in the vertical component of the momentum equation (1), and is in close balance with the non-hydrostatic pressure gradient in the vertical. Any deviation from this balance induces vertical acceleration in the fluid.

On the other hand, we can use either a Smagorinsky model (see [37]) or a constant value for the horizontal turbulent viscosity coefficient ν_{H}, and either a Munk–Anderson model (see [38]), a Pacanowski–Philander model (see [39]) or a homogeneous distribution for the vertical turbulent viscosity coefficient ν_{V}. In addition, centrifugal accelerations that have been incorporated into the gravity term, yielding an effective gravity acceleration that is aligned with the vertical axis.

As is often done in ocean flow models, the evolution of the sea surface is characterized by a function $\eta(x,y,t)$, where $(x,y)\in S$ and $t\in(0,T)$, which represents the elevation of the surface with respect to the reference plane $z=0$. Since in ocean flows the magnitude of the free-surface elevation is much smaller than the average water depth, several ocean models solve the hydrodynamic problem in the fix domain Ω (see, for instance, [12, 15, 21–23]), which is not updated to reflect the variations of the free surface. This is computationally much more economical than other techniques such as purely Lagrangian or ALE formulations (see, for instance, [40]) used in other areas of Computational Fluid Dynamics, since the need for remeshing or moving the mesh in each time step is avoided. The evolution of the free-surface elevation η is governed by the kinematic equation:

$$\frac{\partial\eta}{\partial t}+u\frac{\partial\eta}{\partial x}+v\frac{\partial\eta}{\partial y}=w \quad \text{in } S\times(0,T) \tag{3}$$

Contrary to most of the existing numerical models for free-surface ocean flow problems, we do not integrate the continuity equation (2) vertically along each column of fluid and use condition (3) to derive a vertically averaged free-surface equation. Instead, we solve Equation (3) as it is without any further approximation. This way, the numerical solution will not be affected by errors due to the presence of a slight numerical compressibility in the discrete solution. We believe the resulting scheme will be robust.

Furthermore, it is usual in non-hydrostatic ocean flow models to use some pressure splitting (see [12, 14–17, 19, 21–23]). We decompose the total pressure P in Equation (1) into its atmospheric, hydrostatic and non-hydrostatic components:

$$P(x,y,z,t)=p_a(x,y,t)+g(\eta-z)+p(x,y,z,t) \tag{4}$$

where p_{a} is the atmospheric pressure (which we assume to be zero). Using (4) in (1) results in

$$\begin{aligned}\frac{\partial\mathbf{u}}{\partial t}+(\mathbf{u}\cdot\nabla)\mathbf{u}+\mathbf{k}\times\mathbf{u}+\nabla p-\frac{\partial}{\partial x}\left(\nu_{\mathrm{H}}\frac{\partial\mathbf{u}}{\partial x}\right)&\\ -\frac{\partial}{\partial y}\left(\nu_{\mathrm{H}}\frac{\partial\mathbf{u}}{\partial y}\right)-\frac{\partial}{\partial z}\left(\nu_{\mathrm{V}}\frac{\partial\mathbf{u}}{\partial z}\right)&=-g\nabla_2\eta \quad \text{in } \Omega\times(0,T)\end{aligned} \tag{5}$$

$$\nabla\cdot\mathbf{u}=0 \quad \text{in } \Omega\times(0,T) \tag{6}$$

where $\nabla_2 = (\partial/\partial x, \partial/\partial y, 0)$ is the 2D gradient operator extended to 3D. The pressure splitting (4) allows to incorporate barotropic forcing effects into the hydrodynamical problem through the right-hand-side term in (5). We use Equations (5) and (6) and the kinematic free-surface equation (3) in our model.

Boundary conditions have to be supplied to the equation system (3)–(5)–(6). At the bottom of the domain, which we assume impermeable, the kinematic boundary condition reads as

$$w + u\frac{\partial \mathscr{H}}{\partial x} + v\frac{\partial \mathscr{H}}{\partial y} = 0 \quad \text{on } \Gamma_b \tag{7}$$

so that we can deal with irregular topographies. Moreover, we use a linear dependence on the current for the bottom friction due to rugosity:

$$\nu_{\mathrm{H}} n_x \left(\frac{\partial u}{\partial x}, \frac{\partial v}{\partial x}\right) + \nu_{\mathrm{H}} n_y \left(\frac{\partial u}{\partial y}, \frac{\partial v}{\partial y}\right) + \nu_{\mathrm{V}} n_z \left(\frac{\partial u}{\partial z}, \frac{\partial v}{\partial z}\right) = (\tau_b^x, \tau_b^y) := C_b(u, v) \quad \text{on } \Gamma_b \tag{8}$$

Here, $\mathbf{n} = (n_x, n_y, n_z)$ is the unit outward normal vector to Γ and C_b is the linear bottom friction coefficient.

Although the expression of the stress tensor involves the symmetric part of the gradient of the velocity field, but we are using the gradient itself, tangent wind stress at the free surface is modelled, as usual in ocean models, as

$$\nu_{\mathrm{V}} \left(\frac{\partial u}{\partial z}, \frac{\partial v}{\partial z}\right) = (\tau_s^x, \tau_s^y) := \frac{\rho_a}{\rho_0} C_s (U_{10}^2 + V_{10}^2)^{1/2} (U_{10}, V_{10}) \quad \text{on } \Gamma_s \tag{9}$$

where ρ_a is the air's density, C_s the dimensionless wind drag coefficient and (U_{10}, V_{10}) the horizontal wind velocity vector at a reference height of 10 m above the surface. Zero normal stress is also imposed on Γ_s:

$$\nu_{\mathrm{V}} \frac{\partial w}{\partial z} = 0 \quad \text{on } \Gamma_s \tag{10}$$

Finally, different conditions may be applied on the lateral boundary Γ_l, according to different physical situations; let us write $\Gamma_l = \Gamma_{\mathrm{I}} \cup \Gamma_{\mathrm{W}} \cup \Gamma_{\mathrm{O}}$ (with empty intersections pairwise) corresponding to the inflow, solid wall and outflow parts of that boundary. Then, at inflow a prescribed value of the velocity is imposed:

$$\mathbf{u} = \mathbf{u}_I \quad \text{on } \Gamma_{\mathrm{I}} \tag{11}$$

where $\mathbf{u}_I$ is a given inflow velocity. At solid walls, the impermeability condition is specified, i.e. the velocity normal to the wall is zero, but the fluid may slip tangent to the wall with no tangent stress:

$$n_x u + n_y v = 0 \quad \text{on } \Gamma_{\mathrm{W}} \tag{12}$$

At outflow, zero stress is imposed:

$$\nu_{\mathrm{H}} n_x \frac{\partial \mathbf{u}}{\partial x} + \nu_{\mathrm{H}} n_y \frac{\partial \mathbf{u}}{\partial y} = \mathbf{0} \quad \text{on } \Gamma_{\mathrm{O}} \tag{13}$$

An initial condition must also be specified for the velocity field:

$$\mathbf{u}(x, y, z, 0) = \mathbf{u}^0(x, y, z) \quad \forall (x, y, z) \in \Omega \tag{14}$$

where $\mathbf{u}^0$ is a given 3D, divergence-free initial velocity.

The hydrodynamical model that we consider consists of Equations (3), (5) and (6), boundary conditions (7)–(13) and the initial condition (14). In order to write down the weak form of this problem, which will be needed when we introduce its finite element approximation, and for simplicity of exposition, we will assume in what follows that $\Gamma_l = \Gamma_{\mathrm{I}}$ and $\mathbf{u}_l = \mathbf{0}$, i.e. that the lateral boundary is a closed container where only homogeneous Dirichlet boundary conditions are specified. Then, the velocity $\mathbf{u}$, the non-hydrostatic pressure p and the free-surface elevation η belong, respectively, to the following spaces:

$$V := \left\{ \tilde{\mathbf{u}} = (\tilde{u}, \tilde{v}, \tilde{w}) \in \mathbf{H}^1(\Omega) / \tilde{\mathbf{u}} = \mathbf{0} \text{ on } \Gamma_{\mathrm{I}}, \tilde{w} + \tilde{u}\frac{\partial \mathscr{H}}{\partial x} + \tilde{v}\frac{\partial \mathscr{H}}{\partial y} = 0 \text{ on } \Gamma_b \right\}$$

$$Q := L^2(\Omega)$$

$$M := H^1(S)$$

The weak form of the momentum equation (5) is obtained by multiplying it by a test function $\tilde{\mathbf{u}} = (\tilde{u}, \tilde{v}, \tilde{w}) \in V$, integrating on Ω and making use of Green's formula and the boundary conditions (8), (9) and (10), which yields

$$\begin{aligned}
&\int_\Omega \frac{\partial \mathbf{u}}{\partial t}\tilde{\mathbf{u}}\,\mathrm{d}\Omega + \int_\Omega (\mathbf{u}\cdot\nabla)\mathbf{u}\tilde{\mathbf{u}}\,\mathrm{d}\Omega + \int_\Omega (\mathbf{k}\times\mathbf{u})\tilde{\mathbf{u}}\,\mathrm{d}\Omega + \int_\Omega \nabla p\tilde{\mathbf{u}}\,\mathrm{d}\Omega \\
&\quad + \int_\Omega \left(\nu_{\mathrm{H}}\frac{\partial \mathbf{u}}{\partial x}\frac{\partial \tilde{\mathbf{u}}}{\partial x} + \nu_{\mathrm{H}}\frac{\partial \mathbf{u}}{\partial y}\frac{\partial \tilde{\mathbf{u}}}{\partial y} + \nu_{\mathrm{V}}\frac{\partial \mathbf{u}}{\partial z}\frac{\partial \tilde{\mathbf{u}}}{\partial z} \right) \mathrm{d}\Omega \\
&= -g\int_\Omega \nabla_2\eta\tilde{\mathbf{u}}\,\mathrm{d}\Omega + \int_{\Gamma_s} (\tau_s^x\tilde{u} + \tau_s^y\tilde{v})\,\mathrm{d}\Gamma \\
&\quad + \int_{\Gamma_b} (\tau_b^x\tilde{u} + \tau_b^y\tilde{v})\,\mathrm{d}\Gamma + \int_{\Gamma_b} \mathbf{n}_\nu\cdot\nabla w\tilde{w}\,\mathrm{d}\Gamma
\end{aligned}$$

where (τ_b^x, τ_b^y) are given by (8) and (τ_s^x, τ_s^y) by (9) and we have used the notation $\mathbf{n}_\nu = (\nu_{\mathrm{H}}n_x, \nu_{\mathrm{H}}n_y, \nu_{\mathrm{V}}n_z)$.

The continuity equation (6) is also enforced weakly. In this case, a scalar test function $q \in Q$ is considered, so that multiplying (6) by q and integrating on Ω leads to

$$\int_\Omega (\nabla\cdot\mathbf{u})q\,\mathrm{d}\Omega = 0$$

Finally, the weak form of the free-surface equation (3) is written, for an arbitrary $\mu \in M$, as

$$\int_S \frac{\partial \eta}{\partial t}\mu\,\mathrm{d}\Gamma + \int_S u\frac{\partial \eta}{\partial x}\mu\,\mathrm{d}\Gamma + \int_S v\frac{\partial \eta}{\partial y}\mu\,\mathrm{d}\Gamma = \int_S w\mu\,\mathrm{d}\Gamma$$

3. NUMERICAL APPROXIMATION

We describe in this section the numerical scheme that we employ for the approximation of the hydrodynamical problem (3)–(5)–(6). We first introduce the time-stepping scheme in a semidiscrete (continuous in space) context and we then consider a spatial discretization by the finite element method.

3.1. Time stepping

It is a common practice in non-hydrostatic ocean models to use a fractional-step method as time integration scheme (see, e.g. [15, 16, 18]). In this kind of a method, each time step is decomposed into a number of substeps, generally two (see, for instance, [41, 42] and the references therein). The hydrostatic pressure is split from the non-hydrostatic contribution as in Equation (4); the latter is then neglected in the first fractional step and an intermediate, non-divergence-free velocity field is thus computed. The non-hydrostatic pressure correction is then obtained by projecting the intermediate velocity field onto the subspace of solenoidal vector fields. Although this splitting allows to segregate the calculation of the non-hydrostatic pressure correction from that of the velocity, thus reducing the computational cost, a splitting error is introduced. Moreover, fractional-step methods are known to require stable velocity-pressure approximations in order to yield convergent solutions (see [42]), just as mixed methods do.

As an alternative approach, we employ an implicit backward Euler monolithic method for the time integration of (5)–(6), in which the velocity and the pressure are computed simultaneously (a monolithic time-stepping method was also employed in [23]). The free-surface elevation, however, is treated explicitly in the momentum equation (5), otherwise the dimension of the discrete equation system would increase significantly. The free-surface elevation is updated at the end of the step using the newly calculated velocity field, integrating (3) implicitly once again by the backward Euler method. A similar approach was used in [21] for the treatment of the free-surface elevation. The rest of the terms in the momentum equation (5) are treated implicitly but for the convective (nonlinear) term, which is linearized using the value of the velocity at the previous time-step as convective velocity; this is a simple approximation of first order in the time-step size, which is consistent with the overall accuracy of the method.

Thus, given a time-step size $\Delta t > 0$ and assuming that approximations $\mathbf{u}^n$ of the velocity and η^n of the free-surface elevation at time $t_n = n\Delta t$ are known, a new velocity $\mathbf{u}^{n+1}$ and pressure p^{n+1} at t_{n+1} are obtained from:

$$\begin{aligned}\frac{1}{\Delta t}(\mathbf{u}^{n+1}-\mathbf{u}^n)+(\mathbf{u}^n\cdot\nabla)\mathbf{u}^{n+1}+\mathbf{k}\times\mathbf{u}^{n+1}+\nabla p^{n+1}-\frac{\partial}{\partial x}\left(\nu_{\mathrm{H}}\frac{\partial \mathbf{u}^{n+1}}{\partial x}\right)&\\ -\frac{\partial}{\partial y}\left(\nu_{\mathrm{H}}\frac{\partial \mathbf{u}^{n+1}}{\partial y}\right)-\frac{\partial}{\partial z}\left(\nu_{\mathrm{V}}\frac{\partial \mathbf{u}^{n+1}}{\partial z}\right)=-g\nabla_2\eta^n \quad \text{in } \Omega & \qquad (15)\end{aligned}$$

$$\nabla\cdot\mathbf{u}^{n+1}=0 \quad \text{in } \Omega \qquad (16)$$

Then, a new approximation η^{n+1} of the free-surface elevation at time t_{n+1} is obtained from:

$$\frac{1}{\Delta t}(\eta^{n+1}-\eta^n)+u^{n+1}\left(\frac{\partial\eta}{\partial x}\right)^{n+1}+v^{n+1}\left(\frac{\partial\eta}{\partial y}\right)^{n+1}=w^{n+1} \quad \text{in } S \qquad (17)$$

The weak form of the semidiscrete problem (15)–(16)–(17) consists in finding $\mathbf{u}^{n+1}=(u^{n+1}, v^{n+1}, w^{n+1})\in V$, $p^{n+1}\in Q$ and $\eta^{n+1}\in M$ such that, for all test functions $\tilde{\mathbf{u}}=(\tilde{u}, \tilde{v}, \tilde{w})\in V$, $q\in Q$ and $\mu\in M$:

$$\begin{aligned}
&\int_\Omega \frac{1}{\Delta t}(\mathbf{u}^{n+1}-\mathbf{u}^n)\tilde{\mathbf{u}}\,\mathrm{d}\Omega+\int_\Omega(\mathbf{u}^n\cdot\nabla)\mathbf{u}^{n+1}\tilde{\mathbf{u}}\,\mathrm{d}\Omega+\int_\Omega(\mathbf{k}\times\mathbf{u}^{n+1})\tilde{\mathbf{u}}\,\mathrm{d}\Omega+\int_\Omega\nabla p^{n+1}\tilde{\mathbf{u}}\,\mathrm{d}\Omega\\
&\quad+\int_\Omega\left(v_{\mathrm{H}}\frac{\partial\mathbf{u}^{n+1}}{\partial x}\frac{\partial\tilde{\mathbf{u}}}{\partial x}+v_{\mathrm{H}}\frac{\partial\mathbf{u}^{n+1}}{\partial y}\frac{\partial\tilde{\mathbf{u}}}{\partial y}+v_{\mathrm{V}}\frac{\partial\mathbf{u}^{n+1}}{\partial z}\frac{\partial\tilde{\mathbf{u}}}{\partial z}\right)\mathrm{d}\Omega\\
&=-g\int_\Omega\nabla_2\eta^n\tilde{\mathbf{u}}\,\mathrm{d}\Omega+\int_{\Gamma_s}(\tau_s^x\tilde{u}+\tau_s^y\tilde{v})\,\mathrm{d}\Gamma\\
&\quad+\int_{\Gamma_b}(\tau_b^x(u^{n+1})\tilde{u}+\tau_b^y(v^{n+1})\tilde{v})\,\mathrm{d}\Gamma+\int_{\Gamma_b}\mathbf{n}_v\cdot\nabla w^{n+1}\tilde{w}\,\mathrm{d}\Gamma
\end{aligned}$$

$$\int_\Omega(\nabla\cdot\mathbf{u}^{n+1})q\,\mathrm{d}\Omega=0$$

$$\int_S\frac{1}{\Delta t}(\eta^{n+1}-\eta^n)\mu\,\mathrm{d}\Gamma+\int_S u^{n+1}\left(\frac{\partial\eta}{\partial x}\right)^{n+1}\mu\,\mathrm{d}\Gamma+\int_S v^{n+1}\left(\frac{\partial\eta}{\partial y}\right)^{n+1}\mu\,\mathrm{d}\Gamma=\int_S w^{n+1}\mu\,\mathrm{d}\Gamma$$

3.2. Finite element spatial approximation

3.2.1. Finite element approximation. The semidiscrete problem (15)–(16)–(17) is further discretized in space by the finite element method. We consider an unstructured 2D mesh Σ_h of triangular elements to discretize the surface S. Beneath each triangle, an arbitrary number of prismatic elements is further considered with vertical lateral faces; the top and bottom faces of each prism need not be horizontal and the number of elements in each column need not be constant. We call the resulting 3D mesh Ω_h. This meshing strategy provides full flexibility to approximate both the coastline and the bottom topography. Moreover, each element $K\in\Omega_h$ is the image of the reference prism $\hat{K}:=\hat{T}\times[-1,1]$, where $\hat{T}$ is the simplex of vertices $(0,0)$, $(1,0)$ and $(0,1)$ in $\mathbb{R}^2$, by a mapping F_K that is a tensor product of a polynomial of the first degree in $(\hat{x},\hat{y})$ and a polynomial of the first degree in $\hat{z}$:

$$F_K:\hat{K}\to K \quad \text{with } F_K\in R_1:=P_1((\hat{x},\hat{y}))\otimes P_1(\hat{z})$$

The unknowns of the problem are approximated by finite element functions, which are continuous across interelement boundaries and polynomials within each element when expressed in reference variables $(\hat{x},\hat{y},\hat{z})$. We will focus our attention on the case of equal interpolation for the velocity and the pressure, in which both variables are approximated on the same 3D mesh; the free-surface elevation is approximated by linear polynomials on the 2D mesh Σ_h. The finite element spaces for the approximation of the velocity, the pressure and the free-surface elevation are, respectively,

$$V_h:=\{\tilde{\mathbf{u}}_h\in V/\forall K\in\Omega_h, \tilde{\mathbf{u}}_{h|K}=\hat{\mathbf{u}}_K\circ F_K^{-1}, \hat{\mathbf{u}}_K\in(R_1)^3\}$$

$$Q_h:=\{q_h\in\mathscr{C}^0(\Omega)/\forall K\in\Omega_h, q_{h|K}=\hat{q}_K\circ F_K^{-1}, \hat{q}_K\in R_1\}$$

$$M_h:=\{\mu_h\in\mathscr{C}^0(S)/\forall T\in\Sigma_h, \mu_{h|T}=\hat{\mu}_T\circ F_T^{-1}, \hat{\mu}_T\in S_1\}$$

where $F_T:\hat{T}\to T$ denotes the linear transformation of $\hat{T}$ into T. In these expressions, we have also used the notation:

$$S_1 := P_1(\hat{x},\hat{y})$$

The standard Galerkin approximation of (15)–(16)–(17) consists in finding finite element functions $\mathbf{u}_h^{n+1}=(u_h^{n+1},v_h^{n+1},w_h^{n+1})\in V_h$, $p_h^{n+1}\in Q_h$ and $\eta_h^{n+1}\in M_h$ such that, for all test functions $\tilde{\mathbf{u}}_h=(\tilde{u}_h,\tilde{v}_h,\tilde{w}_h)\in V_h$, $q_h\in Q_h$ and $\mu_h\in M_h$:

$$\begin{aligned}
&\int_\Omega \frac{1}{\Delta t}(\mathbf{u}_h^{n+1}-\mathbf{u}_h^{n})\tilde{\mathbf{u}}_h\,\mathrm{d}\Omega+\int_\Omega(\mathbf{u}_h^{n}\cdot\nabla)\mathbf{u}_h^{n+1}\tilde{\mathbf{u}}_h\,\mathrm{d}\Omega+\int_\Omega(\mathbf{k}\times\mathbf{u}_h^{n+1})\tilde{\mathbf{u}}_h\,\mathrm{d}\Omega\\
&\quad+\int_\Omega\nabla p_h^{n+1}\tilde{\mathbf{u}}_h\,\mathrm{d}\Omega+\int_\Omega\left(\nu_{\mathrm{H}}\frac{\partial\mathbf{u}_h^{n+1}}{\partial x}\frac{\partial\tilde{\mathbf{u}}_h}{\partial x}+\nu_{\mathrm{H}}\frac{\partial\mathbf{u}_h^{n+1}}{\partial y}\frac{\partial\tilde{\mathbf{u}}_h}{\partial y}+\nu_{\mathrm{V}}\frac{\partial\mathbf{u}_h^{n+1}}{\partial z}\frac{\partial\tilde{\mathbf{u}}_h}{\partial z}\right)\mathrm{d}\Omega\\
&=-g\int_\Omega\nabla_2\eta_h^{n}\tilde{\mathbf{u}}_h\,\mathrm{d}\Omega+\int_{\Gamma_s}(\tau_s^x\tilde{u}_h+\tau_s^y\tilde{v}_h)\,\mathrm{d}\Gamma\\
&\quad+\int_{\Gamma_b}(\tau_b^x(u_h^{n+1})\tilde{u}_h+\tau_b^y(v_h^{n+1})\tilde{v}_h)\,\mathrm{d}\Gamma+\int_{\Gamma_b}\mathbf{n}_v\cdot\nabla w_h^{n+1}\tilde{w}_h\,\mathrm{d}\Gamma
\end{aligned}\tag{18}$$

$$\int_\Omega(\nabla\cdot\mathbf{u}_h^{n+1})\tilde{q}_h\,\mathrm{d}\Omega=0\tag{19}$$

$$\begin{aligned}
&\int_S\frac{1}{\Delta t}(\eta_h^{n+1}-\eta_h^{n})\mu_h\,\mathrm{d}\Gamma+\int_S u_h^{n+1}\left(\frac{\partial\eta_h}{\partial x}\right)^{n+1}\mu_h\,\mathrm{d}\Gamma+\int_S v_h^{n+1}\left(\frac{\partial\eta_h}{\partial y}\right)^{n+1}\mu_h\,\mathrm{d}\Gamma\\
&=\int_S w_h^{n+1}\mu_h\,\mathrm{d}\Gamma
\end{aligned}\tag{20}$$

The treatment of the hydrostatic term on the right-hand side of the momentum equation (18) deserves some attention. It involves volume integrals of products of 2D (surface) shape functions (or rather, of their derivatives) and 3D (volume) weighting functions. The calculation of these integrals, which is performed elementwise as is usual in finite element methods, is feasible since we require that the nodes be arranged in columns.

3.2.2. Pressure stabilization. The incompressibility constraint (19) on the velocity field poses a severe problem in the treatment of the pressure. It is well known that if standard approximations are employed in incompressible flow problems, the approximating spaces for the velocity and the pressure have to satisfy a compatibility condition, known as LBB or inf–sup condition, in order to yield a stable and convergent method (see [43]). It needs to be said that equal order interpolations do not satisfy this compatibility condition. Several combinations of finite element spaces for the velocity and for the pressure have been developed which do satisfy it, but stabilized formulations (see [27–30], for instance), which do not require a compatibility condition have proved to be more efficient than stable mixed pairs. In this alternative approach, some terms are added to the discrete problem, which enhance its stability.

A stabilized, finite element formulation for incompressible flow problems was also developed and analyzed in [33, 34] (see also [32, 35]). The main idea of this method consists in introducing a new unknown of the problem that is the orthogonal projection of the gradient of the discrete pressure onto the space of finite element functions. The continuity equation is then modified in a consistent manner by the addition of a suitable multiple of the divergence of the difference between the pressure gradient and its projection. This PGP method was proved in [34] to yield stable and optimally convergent approximate solutions of the steady, incompressible Navier–Stokes equations under a weak condition on the approximating finite element spaces; it was shown in [33] that this condition is satisfied by equal-order interpolations. A similar technique employed together with a backward Euler temporal approximation was shown in [32] to be stable and convergent for the solution of the transient problem.

The stabilized discrete problem that we consider here consists in finding $\mathbf{u}_h^{n+1}=(u_h^{n+1}, v_h^{n+1}, w_h^{n+1})\in V_h$, $p_h^{n+1}\in Q_h$, $\eta_h^{n+1}\in M_h$ and $\mathbf{r}_h^{n+1}=(r_1^{n+1}, r_2^{n+1}, r_3^{n+1})\in R_h$, where

$$R_h=\{\mathbf{s}_h\in(\mathscr{C}^0(\Omega))^3/\forall K\in\Omega_h, \mathbf{s}_{h|K}=\hat{\mathbf{s}}_K\circ F_K^{-1}, \hat{\mathbf{s}}_K\in(R_1)^3\}$$

such that, for all test functions $\tilde{\mathbf{u}}_h=(\tilde{u}_h, \tilde{v}_h, \tilde{w}_h)\in V_h$, $q_h\in Q_h$, $\mu_h\in M_h$ and $\mathbf{s}_h\in R_h$:

$$\begin{aligned}
&\int_\Omega \frac{1}{\Delta t}(\mathbf{u}_h^{n+1}-\mathbf{u}_h^n)\tilde{\mathbf{u}}_h\,\mathrm{d}\Omega+\int_\Omega(\mathbf{u}_h^n\cdot\nabla)\mathbf{u}_h^{n+1}\tilde{\mathbf{u}}_h\,\mathrm{d}\Omega+\int_\Omega(\mathbf{k}\times\mathbf{u}_h^{n+1})\tilde{\mathbf{u}}_h\,\mathrm{d}\Omega+\int_\Omega\nabla p_h^{n+1}\tilde{\mathbf{u}}_h\,\mathrm{d}\Omega\\
&\quad+\int_\Omega\left(v_{\mathrm{H}}\frac{\partial\mathbf{u}_h^{n+1}}{\partial x}\frac{\partial\tilde{\mathbf{u}}_h}{\partial x}+v_{\mathrm{H}}\frac{\partial\mathbf{u}_h^{n+1}}{\partial y}\frac{\partial\tilde{\mathbf{u}}_h}{\partial y}+v_{\mathrm{V}}\frac{\partial\mathbf{u}_h^{n+1}}{\partial z}\frac{\partial\tilde{\mathbf{u}}_h}{\partial z}\right)\mathrm{d}\Omega\\
&=-g\int_\Omega\nabla_2\eta_h^n\tilde{\mathbf{u}}_h\,\mathrm{d}\Omega+\int_{\Gamma_s}(\tau_s^x\tilde{u}_h+\tau_s^y\tilde{v}_h)\,\mathrm{d}\Gamma\\
&\quad+\int_{\Gamma_b}(\tau_b^x(u_h^{n+1})\tilde{u}_h+\tau_b^y(v_h^{n+1})\tilde{v}_h)\,\mathrm{d}\Gamma+\int_{\Gamma_b}\mathbf{n}_v\cdot\nabla w_h^{n+1}\tilde{w}_h\,\mathrm{d}\Gamma
\end{aligned}$$

$$\int_\Omega(\nabla\cdot\mathbf{u}_h^{n+1})\tilde{q}_h\,\mathrm{d}\Omega+\sum_{K\in\Omega_h}\int_K\alpha_K\nabla p_h^{n+1}\nabla q_h\,\mathrm{d}\Omega-\sum_{K\in\Omega_h}\int_K\sqrt{\alpha_K}\mathbf{r}^{n+1}\nabla q_h\,\mathrm{d}\Omega=0$$

$$\int_\Omega\mathbf{r}_h^{n+1}\mathbf{s}_h\,\mathrm{d}\Omega-\sum_{K\in\Omega_h}\int_K\sqrt{\alpha_K}\nabla p_h^{n+1}\mathbf{s}_h\,\mathrm{d}\Omega=0$$

$$\int_S\frac{1}{\Delta t}(\eta_h^{n+1}-\eta_h^n)\mu_h\,\mathrm{d}\Gamma+\int_S u_h^{n+1}\left(\frac{\partial\eta_h}{\partial x}\right)^{n+1}\mu_h\,\mathrm{d}\Gamma+\int_S v_h^{n+1}\left(\frac{\partial\eta_h}{\partial y}\right)^{n+1}\mu\,\mathrm{d}\Gamma=\int_S w_h^{n+1}\mu_h\,\mathrm{d}\Gamma$$

Here, the stability coefficients α_K are computed in terms of the size of elements K, h_K, and a characteristic value of the velocity in elements K, V_K, according to the following expression which is usually employed in stabilized formulations:

$$\alpha_K=\left(c_1\frac{v}{h_K^2}+c_2\frac{V_K}{h_K}+\frac{1}{\Delta t}\right)^{-1}\quad\forall K\in\Omega_h$$

where c_1 and c_2 are given constants.

The meaning of the new variable $\mathbf{r}_h^{n+1}$ can be understood as follows: for continuous finite element interpolations of the pressure p_h^{n+1}, the pressure gradient is a function in $(L^2(\Omega))^3$; $\mathbf{r}_h^{n+1}$ is then the orthogonal projection of the pressure gradient ∇p_h^{n+1} (scaled within each element K by $\sqrt{\alpha_K}$) onto the finite dimensional subspace R_h of $(L^2(\Omega))^3$.

4. NUMERICAL RESULTS

We present in this section some numerical results obtained with the model just described. We first consider two test cases: the problem of wind set-up and the problem of sloshing motion. Then we solve a real-life application problem consisting of the wind-driven circulation in the Bay of Biscay (North of Spain). Other flow problems such as the hydrodynamics in the harbor of Barcelona have been solved satisfactorily with the rigid version of this model (see [44]).

4.1. Wind setup

The term wind setup usually refers to the excess sea levels in the coast generated by a severe wind storm. Physically, the atmosphere acts on the sea in two different ways: changes in atmospheric pressure induce changes in the forces acting vertically on the sea surface, which are felt immediately at all depths; also, forces due to wind stress are generated at and parallel to the sea surface, which controls the downward transfer of momentum. Usually, the effects of winds and pressures cannot be identified separately.

In the simpler setting of a wind of velocity V blowing along a narrow channel of constant depth H, the steady-state effect of the wind stress on the slope of the free surface $\mathrm{d}\eta/\mathrm{d}x$ can be shown to be (see [45]):

$$\frac{\mathrm{d}\eta}{\mathrm{d}x}=\frac{C_s\rho_a V^2}{g\rho H}$$

so that for a channel of length L the setup (height difference between the two ends of the channel due to wind stress) will be $(C_s\rho_a V^2 L)/(g\rho H)$. These expressions highlight the fact that the effect of winds on sea levels increases inversely proportional to the water depth and will be most relevant when the wind blows over extensive regions of coastal shallow water.

We solved this problem on a channel of length $L=1\,\mathrm{m}$, width $W=0.2\,\mathrm{m}$ and depth $H=0.2\,\mathrm{m}$ using a mesh of prismatic elements generated from a surface triangular mesh made up from 40 uniform subdivisions in the x direction (in which the wind is assumed to blow) and 4 subdivisions in the (transversal) y direction; the resulting 160 rectangles are then split into 4 triangles each through their diagonals. In the vertical z direction, 20 non-uniform layers of elements were considered, which are refined near the surface and at the bottom. Thus, the mesh consists of 12 800 prismatic elements and 7665 nodal points. The following values for the physical data were taken for this problem: $C_s=1$, $\rho_a=1\,\mathrm{kg/m^3}$, $\rho=1\,\mathrm{kg/m^3}$ and $g=1\,\mathrm{m/s^2}$, with a wind velocity of $V=1\,\mathrm{m/s}$; for these academical values, the theoretical setup is 5 m. Uniform values of $1\,\mathrm{m^2/s}$ were set for both viscosity coefficients, and Coriolis forces and bottom friction were neglected.

Starting from the fluid at rest with a horizontal initial free surface, a steady-state solution was reached in 313 time steps of size as large as $\Delta t=10\,\mathrm{s}$; a steady-state tolerance of 10^{-4} was allowed in the maximum of the Euclidean norms of the nodal vectors of velocity, pressure and pressure gradient. Figure 1 shows the profile of the free-surface height along the channel centerline $y=0.1\,\mathrm{m}$ at the steady state. An almost linear behavior can be observed, in accordance with theoretical predictions. The strange behavior of the numerical free-surface solution at the left end can be due

DOI: 10.1002/fld

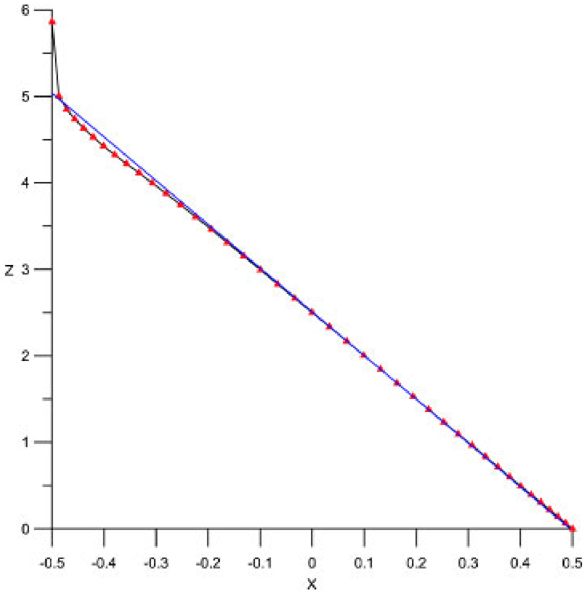

Figure 1. Steady-state profile of the free-surface height along $y=0.1$ in the problem of wind setup and linear regression line of the nodal values.

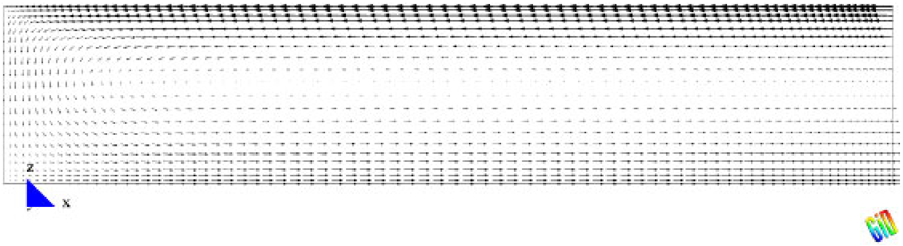

Figure 2. Steady-state velocities along $y=0.1$ in the problem of wind setup.

to the fact that no absorbing condition has been employed at that boundary for the free-surface elevation, which may introduce some reflection. We extrapolated the free-surface height at the end of the channel by a linear regression analysis from the nodal results obtained and found a numerical value for the setup of 5.0575 m, with only 1.15% relative error with respect to the predicted value.

In Figure 2, the steady-state velocities along the section $y=0.1$ m are displayed; a maximum velocity of 0.07 m/s was obtained. In this problem, the use of a non-hydrostatic pressure formulation is needed to obtain a smooth change in the velocity direction near the wall and thus prevent the appearance of oscillations in the velocity field (see [16]); a smooth change in the velocity direction and the absence of oscillations can be clearly observed in Figure 2.

4.2. Water sloshing in a confined container

Water oscillations are one of the natural hazards that can affect harbors, lakes, bays and estuaries. When surface waves are trapped in closed containers, the water level is alternatively high and low at each end of the container with a minimum horizontal flow at those points (the antinodes), whereas at the center (the node) the water level remains constant but the horizontal movement of water is the greatest. Thus, big oscillations in a harbor may dash vessels against the harbor wall or even throw them ashore; at the lowest level at each end, there is also the danger of vessels being grounded, thus suffering damage to their hulls.

Among the different harbor oscillation scenarios, the problem of water sloshing is probably the hardest to solve because of the infinitely many modes that are excited. We simulated a container of length $L=1\,\mathrm{m}$ in the x direction and width $W=0.2\,\mathrm{m}$ in the (transversal) y direction. The still water depth was $H=0.2\,\mathrm{m}$ and the free surface had an initial slope of $S=0.001$ in the x direction; the fluid was initially at rest. Once the fluid begins to move under gravity, there exist an infinite number of standing wave modes in the container. The linear wave theory ensures that the free-surface height can be expressed as

$$\eta(x,t)=\sum_{m=1}^{\infty} A_m \sin(k_m x)\cos(\omega_m t) \tag{21}$$

where

$$k_m=\frac{(2m+1)\pi}{L}, \quad \omega_m=\sqrt{g k_m \tanh(k_m H)} \quad \text{and} \quad A_m=\frac{(-1)^m SL}{(2m+1)^2\pi^2}$$

are the wave number, frequency and amplitude of the mth mode, respectively. A uniform mesh of triangular prismatic elements was used, with $50\times 4\times 10$ subdivisions in the x, y and z directions, respectively; each surface rectangle was split this time into two triangles through one of its diagonals. Thus, there were 5555 nodal points and 8000 finite elements in the mesh. Zero normal flow was imposed on the lateral boundaries and at the bottom. Gravity was set to $g=9.81\,\mathrm{m}^2/\mathrm{s}$, the fluid density was $\rho=1000\,\mathrm{kg/m}^3$ and Coriolis force, wind stress, bottom friction and diffusion were neglected. A time step increment of $\Delta t=10^{-4}\,\mathrm{s}$ was used in order to predict accurately the time evolution of the free surface, and the computation was carried on for two time periods T of the fundamental mode.

Figure 3 shows a comparison of the numerical free-surface profile along $y=0.1$ and the theoretical solution (21) (which is plotted using the first 20 modes) at different times. A very close agreement can be clearly observed at all times, showing that the model proposed is able to reproduce accurately the complex evolution of surface gravity waves. In Figure 4 a 3D view of the free-surface elevation at $t=0.9T$ is shown, where the vertical scale has been magnified 200 times for better visualization; it can be seen that the effect of higher frequency modes is well reproduced numerically.

As the motion of the free surface is not taken into account in the computational domain, one may think that in the proposed scheme the total mass of fluid need not be conserved. In order to check numerically the mass conservation properties of the proposed finite element model, we computed the total mass of fluid obtained in each time step in this problem, the time evolution of which is plotted in Figure 5; as can be observed, the total mass is clearly conserved.

4.3. The Bay of Biscay

Submarine canyons serve as major conduits for nutrient and sediment transport from the land and the continental shelf to the deep sea. The water currents in submarine canyons are generated by many forces, and their presence provides an exchange of shallow shelf water with the deeper water

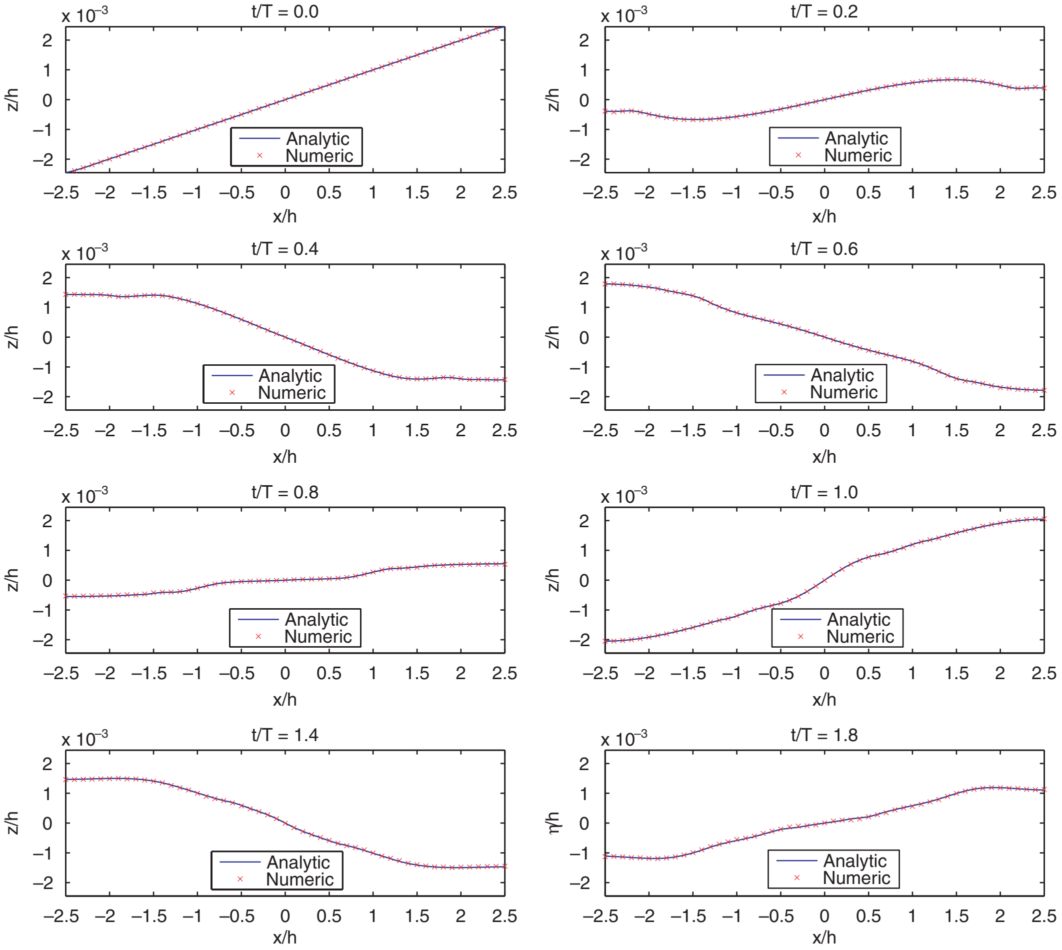

Figure 3. Comparison of the theoretical solution (solid line) and the numerical results (crosses) at different times for the problem of water sloshing.

offshore. In submarine canyons, theoretical models suggest that water circulation is characterized by both downwelling and upwelling events [46] whereas both hydrographic and satellite data indicate the role of these events in the modification of the surface flow [47].

In this third example, the model HELIKE has been used to simulate the current forcing by wind over the Cape Breton Canyon (Figure 6), which is located in the Bay of Biscay in the intersection of the Spanish and French shelves and acts as a front between the French shelf/slope and the Spanish shelf/slope waters. The main feature of the surface water circulation within the area is the presence of the slope circulation named the *Iberian Poleward Current* (IPC). Its direction and location depends upon the prevailing wind regime.

The computational mesh of the study area was generated using the GiD software. The surface representation of the domain is discretized using the advancing front method that is widely used to generate triangular and tetrahedral meshes. To construct the 3D mesh, each node of the previously

DOI: 10.1002/fld

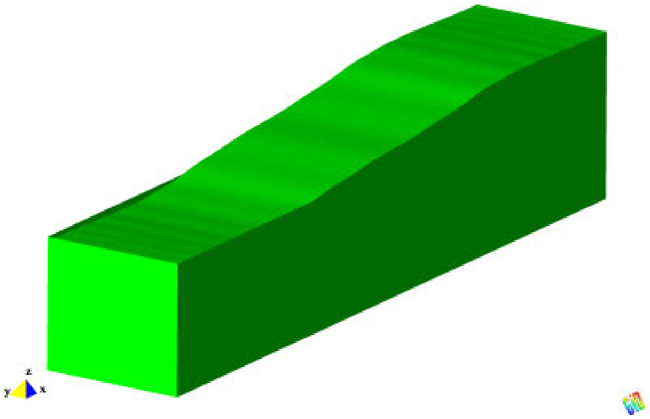

Figure 4. Three-dimensional view of the free-surface elevation at $t=0.9T$ for the problem of water sloshing.

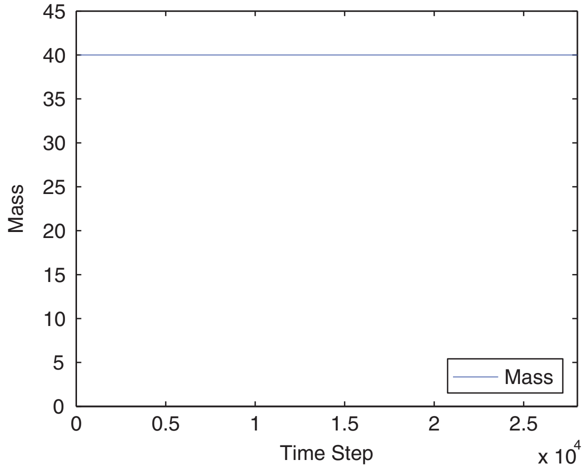

Figure 5. Time evolution of the total mass of fluid for the problem of water sloshing.

generated 2D mesh is projected vertically until it reaches the bottom as shown in Figure 7. All lateral faces of the resulting triangular prisms must be vertical to comply with the numerical requirements of barotropic and baroclinic problems. The superior and inferior bases of the generated triangular prisms are not necessarily horizontal. The final 3D computational grid used has 27 162 nodes, 39 680 elements and five vertical layers.

Since the focus of this numerical test is on the wind-induced circulation, the density field plays no role and has been considered homogeneous with a value of $1025.34\,\mathrm{kg/m^3}$. A wind stress forcing was imposed over the surface boundary, utilizing a wind stress field associated to a SW wind event with a mean wind velocity of $10\,\mathrm{m/s}$.

Two wind-driven experiments were performed. In the first case, a rigid-lid surface boundary condition was applied and in the second case, the free-surface equation was included and the

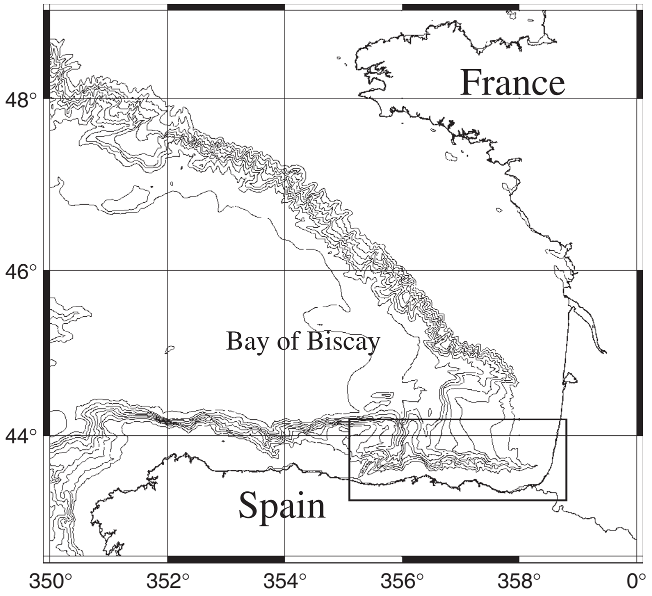

Figure 6. Bay of Biscay: localization and model domain.

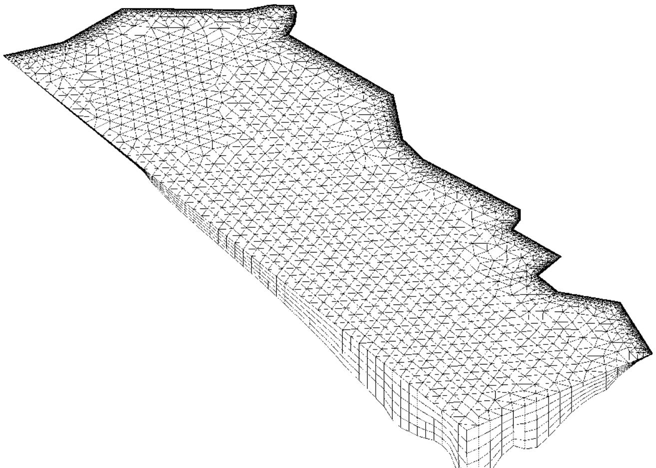

Figure 7. Computational mesh with 27 162 nodes and 39 680 triangular prismatic elements in five layers. The depth is magnified five times for visualization purposes.

barotropic model was used. For both case studies, homogeneous Neumann conditions have been imposed for the flow on the northern and the western boundaries and a no-slip condition has been adopted for the bottom and the coastal contour.

Moreover, simulations were executed until a steady state was reached, with a relative error of 10^{-3}. In the first case, 658 time-steps were employed with a time-step size of 1 s, while in the

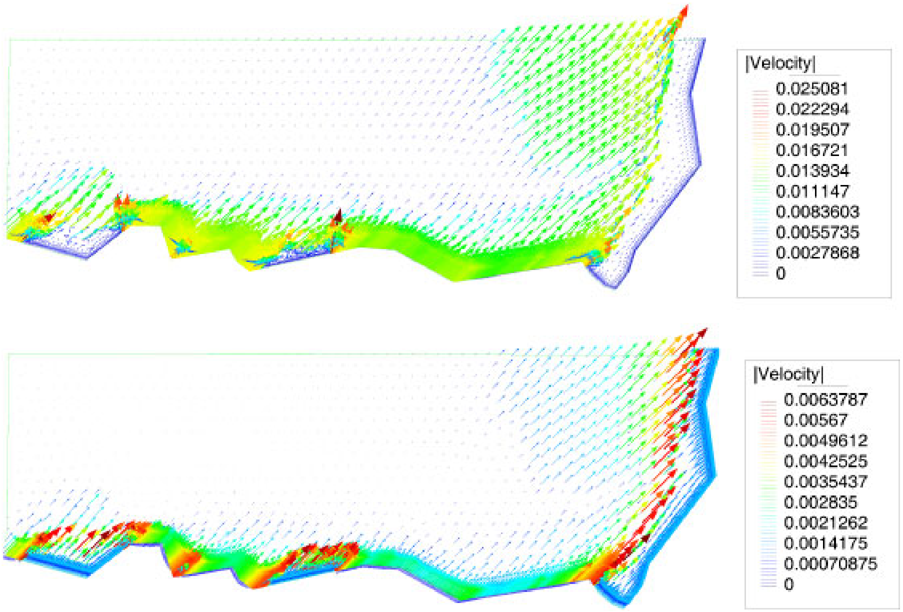

Figure 8. Comparison of the surface velocity field with the rigid-lid (top) and the free-surface (bottom) models.

second case 766 time steps were performed with a time step size of 0.1 s. A Smagorinsky model was used for the horizontal turbulent viscosity coefficient, and a constant value of $10^{-1}\,\mathrm{m}^2/\mathrm{s}$ for the vertical one.

The wind-induced surface velocity field obtained in both cases is shown in Figures 8 and 9 in the form of velocity vectors and their magnitude, respectively. It depends mainly on two factors: the wind direction, which plays an important role in the shallow water areas, and the non-hydrostatic pressure effects due to the canyon slope (see Figure 10), which are observed to be more important in deeper water depths. However, a coastal jet develops only in the free-surface case.

At a depth of 1000 m, the presence of the canyon has more influence on the water circulation (see Figures 11 and 12), but it is only in the free-surface case that the velocity field flows upwards to the upper regions of the submarine canyon, feeding the upwelling. In the lower part of the canyon, some downwelling flow occurs but it is weaker compared with the magnitude of the upwelling flow in the upper part. These results are in agreement with the previous studies and observations conducted by Boyer *et al.* see [48].

5. CONCLUSIONS

The model HELIKE has been developed for the numerical simulation of 3D non-hydrostatic coastal flows with a free surface. This model uses 3D prismatic finite elements with nodes arranged vertically and a pressure stabilization technique, which allows one to employ equal interpolation for the 3D velocities and the pressure. The use of unstructured triangular meshes on the free

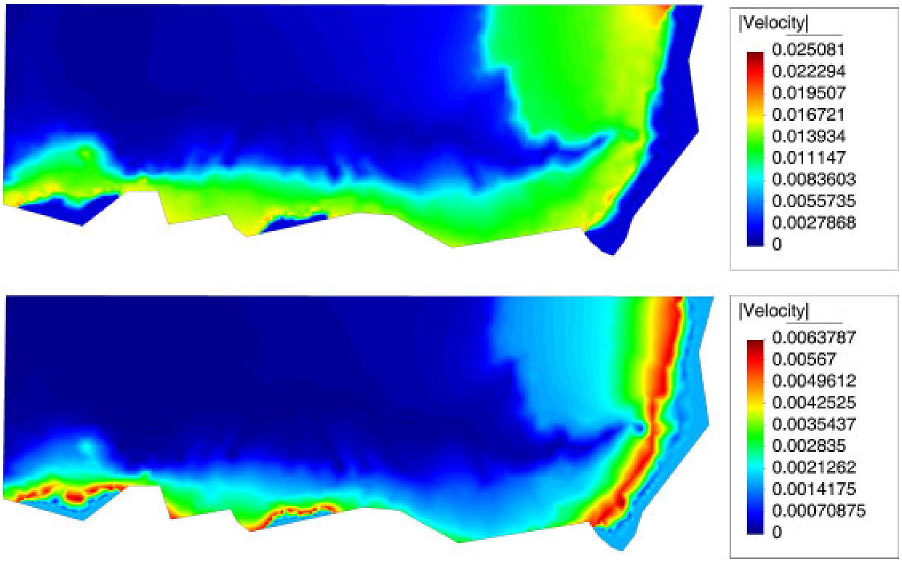

Figure 9. Comparison of the module of the surface velocity field with the rigid-lid (top) and the free-surface (bottom) models.

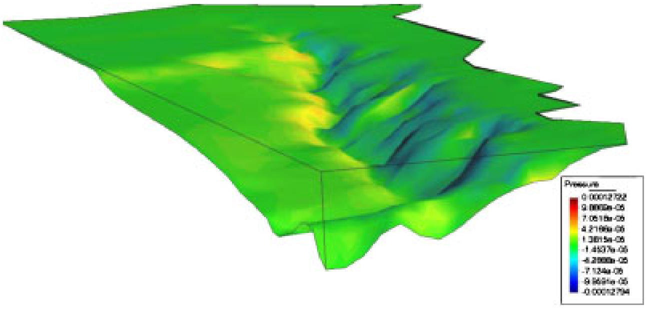

Figure 10. Distribution of the non-hydrostatic pressure field over the Cape Breton Canyon bathymetry in the free-surface case.

surface provides full flexibility to approximate the complex geometry of coastlines, river banks and isobaths. The model also incorporates Coriolis effects, bottom friction, wind stress and different turbulence closure models, and it is applicable to irregular bottom topographies. This model can thus be described as a complete, fully 3D, stabilized finite element, unstructured mesh, non-hydrostatic, free-surface coastal model.

The model HELIKE has proved to reproduce accurately the evolution of surface gravity waves, barotropic effects and wind-driven flows, which frequently occur in coastal ocean flow problems. Some improvements can be envisaged in order to broaden the range of the applicability of the model, such as the incorporation of baroclinic terms. Other practical applications of the model have already been initiated.

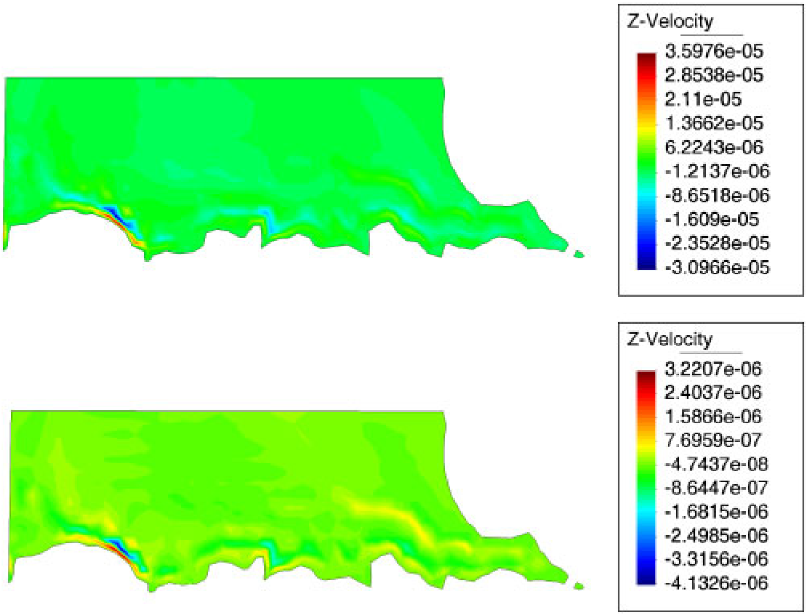

Figure 11. Comparison of the vertical velocity component with the rigid-lid (top) and the free-surface (bottom) models at 1000 m depth.

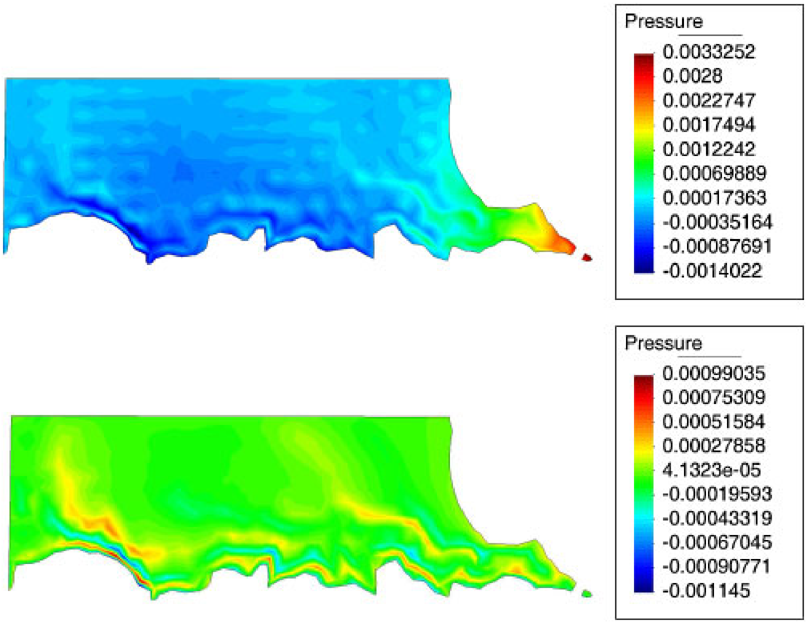

Figure 12. Comparison of the non-hydrostatic pressure with the rigid-lid (top) and the free-surface (bottom) models at 1000 m depth.

ACKNOWLEDGEMENTS

The first author's work was supported by the Spanish MEC under Projects MTM2005-07660-C02-01 and MTM2006-07932. The second and third authors' work was supported by Project MODEGG CTM2005-05410-C03-01.

REFERENCES

1. Sánchez-Arcilla A. Hydrodynamic analysis of the surf zone. *International Journal for Numerical Methods in Engineering* 1989; **27**:87–101.
2. Bermejo R. A finite-element model of two-layer ocean circulation. *International Journal for Numerical Methods in Engineering* 1990; **29**:665–678.
3. Dawson C, Proft J. Coupled discontinuous and continuous Galerkin finite element methods for the depth-integrated shallow water equations. *Computer Methods in Applied Mechanics and Engineering* 2004; **193**:289–318.
4. Espino M, Maidana MA, Sánchez-Arcilla A, German A. Hydrodynamics in the Huelva estuary. Tidal model calibration using field data. *Journal of Waterway*, *Port*, *Coastal and Ocean Engineering* 2007; **133**:313–323.
5. Espino M, Sánchez-Arcilla A, García MA. Wind-induced mesoscale circulation off the Ebro delta, NW Mediterranean: a numerical study. *Journal of Marine Systems* 1998; **16**:235–251.
6. Macías J, Parés C, Castro MJ. Improvement and generalization of a finite element shallow-water solver to multi-layer systems. *International Journal for Numerical Methods in Fluids* 1999; **31**:1037–1059.
7. Maidana MA, Naudin JJ, Espino M, García MA, Sánchez-Arcilla A. Feasibility and usefulness of diagnostic calculations of the mean circulation in the vicinity of the Ebro mouth. Model tests against field data. *Continental Shelf Research* 2002; **22**:229–245.
8. Ortiz P, Zienkiewicz OC, Szmelter J. Hydrodynamics and transport in estuaries and rivers by the CBS finite element method. *International Journal for Numerical Methods in Engineering* 2006; **66**:1569–1586.
9. Wilders P, Stelling GS, van Stijn ThL, Fokkema GA. A fully implicit splitting method for accurate tidal computation. *International Journal for Numerical Methods in Engineering* 1988; **26**:2707–2721.
10. Zienkiewicz OC, Ortíz P. A split-characteristic based finite element model for the shallow water equations. *International Journal for Numerical Methods in Fluids* 1995; **20**:1061–1080.
11. Chacón Rebollo T, Rodríguez Gómez D. A stabilized space-time discretization for the primitive equations in oceanography. *Numerische Mathematik* 2004; **98**:427–475.
12. Danilov S, Kivman G, Schröter J. A finite-element ocean model: principles and evaluation. *Ocean Modelling* 2004; **6**:125–150.
13. Guillén-González F, Rodríguez-Gómez D. Bubble finite elements for the primitive equations of the ocean. *Numerische Mathematik* 2005; **101**:689–728.
14. Iskandarani M, Haidvogel DB, Levin JC. A three-dimensional spectral element model for the solution of the hydrostatic primitive equations. *Journal of Computational Physics* 2003; **186**:397–425.
15. Casulli V, Zanolli P. Semi-implicit numerical modelling of nonhydrostatic free-surface flows for environmental problems. *Mathematical and Computer Modelling* 2002; **36**:1131–1149.
16. Koçyigit MB, Falconer RA, Lin B. Three-dimensional numerical modelling of free surface flows with non-hydrostatic pressure. *International Journal for Numerical Methods in Fluids* 2002; **40**:1145–1162.
17. Lee JW, Teubner MD, Nixon JB, Gill PM. A 3D non-hydrostatic pressure model for small amplitude free-surface flows. *International Journal for Numerical Methods in Fluids* 2006; **50**:649–672.
18. Lin P, Li CW. A σ-coordinate three-dimensional numerical model for surface wave propagation. *International Journal for Numerical Methods in Fluids* 2002; **38**:1045–1068.
19. Stelling G, Zijlema M. An accurate and efficient finite-difference algorithm for non-hydrostatic free-surface flow with application to wave propagation. *International Journal for Numerical Methods in Fluids* 2003; **43**:1–23.
20. Yuan H, Wu CH. An implicit three-dimensional fully non-hydrostatic model for free-surface flows. *International Journal for Numerical Methods in Fluids* 2004; **46**:709–733.
21. Deponti A, Pennati V, De Biase L. A fully 3D finite volume method for incompressible Navier–Stokes equations. *International Journal for Numerical Methods in Fluids* 2006; **852**:617–638.
22. Causin P, Miglio E, Saleri F. Algebraic factorizations for 3D non-hydrostatic free surface flows. *Computing and Visualization in Science* 2002; **5**:85–94.
23. Labeur RJ, Pietrzak JD. A fully three dimensional unstructured grid non-hydrostatic finite element coastal model. *Ocean Modelling* 2005; **10**:51–67.

24. Walters RA. Coastal ocean models: two useful finite element methods. *Continental Shelf Research* 2005; **25**: 775–793.
25. Walters RA. Design considerations for a finite element coastal ocean model. *Ocean Modelling* 2006; **15**:90–100.
26. Barrenechea G, Valentin F. An unusual stabilized finite element method for a generalized Stokes problem. *Numerische Mathematik* 2002; **92**:635–677.
27. Brezzi F, Douglas J. Stabilized mixed methods for the Stokes problem. *Numerische Mathematik* 1988; **53**:225–235.
28. Chacón Rebollo T. A term-by-term stabilization algorithm for the finite element solution of incompressible flow problems. *Numerische Mathematik* 1998; **79**:283–319.
29. Franca LP, Frey SL. Stabilized finite element methods: II. The incompressible Navier–Stokes equations. *Computer Methods in Applied Mechanics and Engineering* 1992; **99**:209–233.
30. Franca LP, Hughes TJR. Convergence analyses of Galerkin least-squares methods for symmetric advective–diffusive forms of the Stokes and incompressible Navier–Stokes equations. *Computer Methods in Applied Mechanics and Engineering* 1993; **105**:285–298.
31. Norburn S, Silveser D. Stabilized vs. stable mixed methods for incompressible flows. *Computer Methods in Applied Mechanics and Engineering* 1998; **166**:131–141.
32. Blasco J, Codina R. Space and time error estimates for a first order, pressure stabilized finite element method for the incompressible Navier–Stokes equations. *Applied Numerical Mathematics* 2001; **38**:475–497.
33. Codina R, Blasco J. A finite element formulation for the Stokes problem allowing equal velocity–pressure interpolation. *Computer Methods in Applied Mechanics and Engineering* 1997; **143**:373–391.
34. Codina R, Blasco J. Analysis of a pressure-stabilized finite element approximation of the stationary Navier–Stokes equations. *Numerische Mathematik* 2000; **87**:59–81.
35. Codina R, Blasco J, Buscaglia GC, Huerta A. Implementation of a stabilized finite element formulation for the incompressible Navier–Stokes equations based on a pressure gradient projection. *International Journal for Numerical Methods in Fluids* 2001; **37**:419–444.
36. Mahadevan A, Oliger J, Street R. A non-hydrostatic mesoscale ocean model. Part I: well-posedness and scaling. *Journal of Physical Oceanography* 1996; **26**:1868–1880.
37. Smagorinsky J. General circulation experiments with the primitive equation: I. The basic experiment. *Monthly Weather Review* 1963; **91**:99–164.
38. Munk WH, Anderson ER. Notes on a theory of the termocline. *Journal of Marine Research* 1948; **7**:276–295.
39. Pacanowski RC, Philander SGH. Parameterization of vertical mixing in numerical models of tropical oceans. *Journal of Physical Oceanography* 1981; **11**:1443–1451.
40. Girault V, López H, Maury B. One time-step finite element discretization of the equation of motion of two-fluid flows. *Numerical Methods for Partial Differential Equations* 2006; **22**:680–707.
41. Blasco J, Codina R, Huerta A. A fractional-step method for the incompressible Navier–Stokes equations related to a predictor–multicorrector algorithm. *International Journal for Numerical Methods in Fluids* 1998; **28**:1391–1419.
42. Guermond JL, Quartapelle L. On stability and convergence of projection methods based on pressure Poisson equation. *International Journal for Numerical Methods in Fluids* 1998; **26**:1039–1053.
43. Brezzi F, Fortin M. *Mixed and Hybrid Finite Element Methods*. Springer Series in Computational Mathematics, vol. 15. Springer: Berlin, 1991.
44. Grifoll M, Espino M, Maidana A, Blasco J, Sánchez-Arcilla A. Estudio numérico tridimensional de la hidrodinámica del puerto de Barcelona como apoyo a su gestión medioambiental. *Proceedings of the VI Congreso de Métodos Numéricos en Ingeniería*, Granada, Spain, 2005. Sociedad Española de Métodos Numéricos en Ingeniería and Associaçao Portuguesa de Mecânica Teórica. ISBN: 84-95999-74-9.
45. Pugh DT. *Tides, Surges and Mean Sea-level*. Wiley: New York, 1987.
46. Puig P, Palanques A, Guillén J, García-Ladona E. Deep slope currents and suspended particle fluxes in and around the Foix submarine canyon (NW Mediterranean). *Deep-sea Research I* 2000; **47**:343–366.
47. Masó M, La Violette PE, Tintoré J. Coastal flow modification by submarine canyons along the NE Spanish coast. *Scientia Marina* 1990; **54**:343–348.
48. Boyer DL, Haidvogel DB, Pérenne N. Laboratory-numerical model comparisons of canyon flows: a parameter study. *Journal of Physical Oceanography* 2004; **34**:1588–1609.

DOI: 10.1002/fld